WILEY-VCH

RESEARCH ARTICLE

ADVANCED FUNCTIONAL MATERIALS
www.afm-journal.de

Realizing Simultaneous X-Ray Imaging and Dosimetry Using Phosphor-Based Detectors with High Memory Stability and Convenient Readout Process

Zetian Yang, Jieqi Hu, David Van der Heggen, Ang Feng, Hairong Hu, Henk Vrielinck, Philippe F. Smet, and Dirk Poelman**

DOI: 10.1002/adfm.202201684

Realizing simultaneous X-ray Imaging and Dosimetry using Phosphor-based Detectors with High Memory Stability and Convenient Readout Process

Zetian Yang, Jieqi Hu, David Van der Heggen, Ang Feng, Hairong Hu, Henk Vrielinck, Philippe F. Smet, Dirk Poelman**

Z. Yang, J. Hu, Dr. D. Van der Heggen, A. Feng, Dr. H. Hu, Prof. P. F. Smet, Prof. D. Poelman
LumiLab, Department of Solid State Sciences, Ghent University, Krijgslaan 281-S1, Ghent B-9000, Belgium
E-mail: david.vanderheggen@ugent.be; dirk.poelman@ugent.be

Dr. H. Hu
Hunan Provincial Key Laboratory of Advanced Materials for New Energy Storage and Conversion, Hunan University of Science and Technology, Xiangtan 411201, Hunan, China

Prof. H. Vrielinck
Electron Magnetic Resonance Group, Department of Solid State Sciences, Ghent University, Krijgslaan 281-S1, B-9000, Ghent, Belgium

Keywords: X-ray storage phosphors, X-ray detectors, X-ray imaging, dosimetry, radiation-induced valence change, luminescence

Flexible X-ray storage phosphor sheets are regarded as promising alternatives to conventional electronic flat-panel X-ray detectors, enabling X-ray imaging and dosimetry in less accessible situations. However, it is a challenge to develop phosphor-based detectors with high memory stability and convenient readout processes. Here, we demonstrate an approach to realize this using radiation-induced photoluminescence tuning in $(Ba_{1-x}Sr_x)_2SiO_4$:Eu phosphors, ascribed to the reduction of Eu^{3+} towards Eu^{2+}. The associated photoluminescence spectral change and the accompanying color contrast in response to the radiation dose are exploited for simultaneous X-ray dosimetry and imaging. The recorded image can be read out conveniently by a regular photo camera upon UV illumination and the radiation dose can be extracted during the imaging process in a ratiometric way via the green to red pixel intensity, avoiding the need for an absolute intensity measurement. Moreover, the imaged information can maintain for longer

than 28 days and the plate can be reused for X-ray detection after bleaching upon 420 nm illumination, exhibiting superior memory retention ability and good cycling resistance. These results reveal the great potential of $(Ba_{1-x}Sr_x)_2SiO_4$:Eu for X-ray based microbeam radiation therapy and nondestructive inspection and are expected to stimulate the research on phosphor-based photoluminescence modulated detectors.

1. Introduction

Since its discovery by Wilhelm Röntgen in 1895, X-rays have been utilized in multiple critical fields ranging from medical diagnostics to safety inspection and (non-destructive) crack detection.[1-4] For these applications, photodetectors that allow for high-quality X-ray imaging and accurate X-ray dosimetry are highly desired and significant efforts have been made to design such detectors in recent years.[5-7] The current real-time X-ray detection technologies mainly work on two different principles: direct conversion of X-ray energy into electrical charges using semiconductors,[8-14] and indirect conversion of X-ray energy into ultraviolet or visible light using scintillators and subsequent detection by photodiodes.[15-27] Despite their high sensitivity and low detection limit, the widespread applicability of these X-ray detectors is hampered by their high cost, small dimensions, time-consuming production processes and complex system configuration. Moreover, these technologies require integration with thin-film transistors consisting of pixelated photodiode arrays to form the so-called flat-panel X-ray detectors in practical applications. To directly image irregular objects, a flexible detector is required which is difficult to achieve for this type of detector.[28, 29]

X-ray storage phosphor-based detectors are considered as a promising alternative to flat-panel X-ray detectors owing to their simple configuration, flexible structure, low cost and large area.[29, 30] These X-ray storage phosphors are a kind of luminescent material exhibiting stable charge storage after absorption of ionizing radiation.[31] Upon external stimulation, charge carriers can be de-trapped and then recombine at the luminescent centers to emit light with an intensity that is proportional to the radiation dose. Depending on whether the external stimulus is an increased temperature or electromagnetic radiation, the corresponding de-trapping process is referred to as thermoluminescence (TL) or optically stimulated luminescence (OSL).[32-34] Up to now, a variety of phosphor-based X-ray detectors have been reported which are either optically or thermally read out.[30, 35-39] Among them, the most representative and commercially used one is BaFBr:Eu^{2+}, especially for the application in computed radiography.[31] Under X-ray irradiation, a latent image of the object is first formed in a BaFBr:Eu^{2+} plate and then the readout is performed upon 633 nm laser stimulation.[35, 40] Despite good stability, the

information readout process requires point by point scanning of the plate and collection of the emitted blue light with the assistance of a photomultiplier, which is time-consuming and less convenient in practical applications. To overcome this problem, Ou *et al*. recently developed $NaLuF_4$:Tb persistent luminescent phosphors for X-ray imaging and called this X-ray luminescence extension imaging.[29] Van der Heggen *et al.* showed earlier in similar $Na(Lu,Gd)F_4$:Tb persistent luminescent particles embedded in a flexible binder that an X-ray dose could be determined by thermal or optical read-out.[41] However, the luminescence intensity gradually decays after switching off the X-ray source, making the recorded information unstable. Although the already high afterglow lifetime of $NaLuF_4$:Tb nanoparticles was significantly prolonged through coating with a $NaYF_4$ shell, this instability is inconvenient in practical applications.[29, 41] In addition, for medical applications it is highly desirable to accurately estimate the irradiation dose during X-ray treatments, which is important for patient safety since excessive X-ray dose may induce some new diseases like skin damage, alopecia and even cancer.[42-44] In microbeam radiation therapy, for example, it is necessary to first measure the distribution of the radiation dose before actual use. The large variation in radiation dose between the centers of the microbeams, where doses can reach hundreds or thousands of grays, and the valleys of beams where the doses are of the order of a few dozens of grays,[45] is especially challenging for the existing radiation detectors which cannot satisfy the requirements in terms of both the large dose range and microscale distribution. As a result, the development of new, stable phosphor-based detectors enabling simultaneous X-ray imaging and dosimetry is of major interest. Furthermore, avoiding the need for absolute intensity measurements to accurately determine the dose would enable the use of those phosphor-based detectors in more challenging and less accessible environments.

In some phosphors, the charge storage is accompanied by a radiation-induced valence change of the dopants upon X-ray irradiation, generating a new type of luminescent center.[46, 47] Both the emission intensity of the radiation-induced luminescent center and the photoluminescence color of the phosphor can then be radiation dose-dependent which can be employed for combined X-ray dosimetry and imaging. If the recorded signal is stable after X-ray irradiation and when it can be conveniently read out upon UV illumination using the photoluminescence color contrast, it can overcome the shortcomings of complex readout processes or poor memory stability of X-ray storage phosphors previously reported. However, it should be mentioned that although the phenomenon of radiation-induced photoluminescence change has been observed in some phosphors such as KBr:Sm, $BaLiF_3$:Sm and ZnS:Mn,Eu,[48-50] their emission wavelengths before and after irradiation usually overlap or their excitation

and emission wavelengths are close to each other. This results in high uncertainty and hence limits their applicability for high energy detection. In contrast, a strongly different photoluminescence spectrum is observed in $(Ba_{1-x}Sr_x)_2SiO_4$:Eu phosphors after X-ray irradiation due to the reduction of Eu^{3+} towards Eu^{2+}, as confirmed by Volhard *et al*. and Nag *et al*.[51, 52] This behavior indicates that $(Ba_{1-x}Sr_x)_2SiO_4$:Eu would be a promising phosphor for X-ray detection.

In this work, we demonstrate a phosphor-based X-ray detector with the ability of simultaneous X-ray imaging and dosimetry based on radiation-induced photoluminescence tuning in $(Ba_{1-x}Sr_x)_2SiO_4$:Eu (x = 0, 0.5 and 1). The X-ray imaging and dosimetry processes are presented in **Figure 1**. Upon exposure, the X-rays penetrating the object will irradiate the image plate, forming a latent image. The image can be read out directly upon UV illumination because of the distinct photoluminescence color contrast of the plate after receiving different irradiation doses. This is most outspoken for Ba_2SiO_4:Eu, where the emission color changes from red to green upon irradiation, and the radiation dose can be accurately extracted from the color coordinates of the X-ray image, showing the capability of simultaneous X-ray imaging and dosimetry. Meanwhile, compared with previously reported detectors, the readout process of Ba_2SiO_4:Eu-based detectors does not require any expensive or specialized equipment and is independent of the excitation intensity, thereby avoiding the need for absolute emission intensity measurements, which is convenient in practical applications. Furthermore, the recorded image can be completely erased upon 420 nm irradiation and then the device can be reused for X-ray detection. The high radiation resistance and large dose range endow Ba_2SiO_4:Eu detectors with great potential for microbeam radiation therapy, flash radiotherapy, food irradiation and detection of highly radioactively-contaminated areas where high integrated doses and large dose ranges are regularly encountered.[45, 53] These excellent properties confirm the feasibility of using radiation-induced luminescence tuning in phosphors for simultaneous X-ray imaging and dosimetry. More importantly, our findings open a new window to design phosphor-based X-ray detectors with high memory stability and convenient readout processes.

2. Results and Discussion

A pure orthorhombic structure with a Pnma space group was formed in all synthesized phosphors. A comparison to the reference cards of PDF#26-1403 (Ba_2SiO_4) and PDF#39-1256 (Sr_2SiO_4) indicate that the Eu^{3+} ions incorporate into the $(Ba_{1-x}Sr_x)_2SiO_4$ lattice and do not form a separate phase, irrespective of the synthesis atmosphere (see **Figure 2**a). The crystal structure of Ba_2SiO_4 is shown in Figure 2b, where Ba^{2+} occupies two types of lattice sites, with a 10-fold

and a 9-fold coordinated oxygen-polyhedron, respectively. According to the ionic radius and coordination number of Ba^{2+} (1.47 Å, CN = 9), Sr^{2+} (1.31 Å, CN = 9), Si^{4+} (0.26 Å, CN = 4) and Eu^{3+} (1.12 Å, CN = 9),[54] the Eu^{3+} ions are expected to replace Ba^{2+} or Sr^{2+} ions.[55] The scanning electron microscope (SEM) image shows that Ba_2SiO_4:Eu exhibits a dense microstructure with some irregular-shaped particles (see Figure S1a). The average grain size was 16.6 ± 0.9 μm exhibiting a broad distribution between 5 μm and 30 μm (see Figure S1b), and the elements of Ba, Si and Eu were homogeneously distributed in the Ba_2SiO_4:Eu (see Figure S1c). These results evidence that the prepared samples possess a pure phase with a high crystalline quality.

Room-temperature photoluminescence emission (PL) and excitation (PLE) spectra of $(Ba_{1-x}Sr_x)_2SiO_4$:Eu before X-ray irradiation are shown in Figure 2c. Monitoring the PL emission at 612 nm, all of the PLE spectra consist of a broad $O^{2-} \rightarrow Eu^{3+}$ charge transfer (CT) band in the range 235 - 335 nm and a series of narrow lines originating from $4f^6$-$4f^6$ transitions of Eu^{3+}. Upon 392.5 nm excitation, the PL spectra of all samples exhibit several peaks in the range from 575nm to 725nm corresponding to the $^5D_0 \rightarrow {}^7F_J$ (J=0, 1, 2, 3, 4) transitions of Eu^{3+}, respectively. The peak of the CT band gradually shifts to higher energy with an increasing Sr content (see Figure S2). After X-ray irradiation, an additional broad emission band emerges in $(Ba_{1-x}Sr_x)_2SiO_4$:Eu phosphors, centered at 506 nm, 520 nm and 550 nm for x=0, 0.5 and 1, respectively (Figure 2d and Figure S3). It can be attributed to the allowed $4f^6 5d^1 \rightarrow 4f^7$ transition of Eu^{2+} ions which originate from the reduction of Eu^{3+} upon X-ray irradiation.[51, 52] For the $4f^6 5d^1 \rightarrow 4f^7$ transition, the 5d orbitals are strongly affected by the surrounding chemical environment. With an increasing Sr content, the crystal field splitting increases because of the smaller ionic radius of Sr^{2+} compared to the radius of Ba^{2+}, and a red-shift of the emission wavelength is observed accordingly.[56, 57] Compared to $BaSrSiO_4$:Eu and Sr_2SiO_4:Eu, there is a larger separation between the emission band of Eu^{2+} and the emission lines of Eu^{3+} in Ba_2SiO_4:Eu, thereby avoiding any overlap. Figure 2e shows the electron paramagnetic resonance (EPR) spectra of Ba_2SiO_4:Eu sintered in air before and after X-ray irradiation and Ba_2SiO_4:Eu sintered in reducing atmosphere. A strong signal of Eu^{2+} was observed in Ba_2SiO_4:Eu sintered in reducing atmosphere, while the signal of Eu^{2+} only appears after X-ray irradiation for Ba_2SiO_4:Eu sintered in air. This confirms that Eu in Ba_2SiO_4:Eu sintered in air is trivalent and a fraction of Eu^{3+} ions is reduced to Eu^{2+} upon X-ray irradiation. In addition, the EPR spectrum of Ba_2SiO_4:Eu sintered in a reducing atmosphere was simulated, which can be well reproduced with only a single set of Eu^{2+} spin Hamiltonian parameters (see Figure S4). This result indicates that Eu^{2+} ions only occupy one type of lattice site in Ba_2SiO_4:Eu, which is

in agreement with previous results.[55] The strong signal at 1212 mT (g = 2.0032) may come from free carbon-centered radicals produced during the sintering. When the unpaired spin is partially delocalized onto neighboring oxygen, shifts from the free-electron g value (2.0023) may indeed be expected for such radicals.[58] The identical emission spectra of Ba_2SiO_4:Eu sintered in air after X-ray irradiation and sintered in reducing atmosphere in combination with the EPR results indicate that that Eu^{2+} ions are formed in the host upon X-ray irradiation (see Figure 2f).

This remarkable photoluminescence change is observed for all compositions and this special behavior gives $(Ba_{1-x}Sr_x)_2SiO_4$:Eu phosphors the potential to be used for X-ray dosimetry through detecting the emission intensity of Eu^{2+} and/or Eu^{3+}. To evaluate the feasibility of the method, *in situ* PL measurements of $(Ba_{1-x}Sr_x)_2SiO_4$:Eu phosphors as a function of X-ray irradiation time were carried out. Here, the X-ray dose is linear to the irradiation time with a fixed dose rate of 15 Gy min^{-1}. A 365 nm light emitting diode with a band pass filter (see Figure S5 for the spectrum) was selected as the PL excitation source since it can excite both Eu^{2+} and Eu^{3+}. However, the light used for excitation can also bleach the sample and hence the dependence of the emission intensity of Eu^{2+} or Eu^{3+} as a function of radiation time will be slightly different for a different excitation wavelength (see Figure S6), which means that for practical applications the relationship between the emission intensity of Eu^{2+} or Eu^{3+} and the radiation time needs to be established first for the specific excitation wavelength used. Figure S7 presents the schematic setup of the *in situ* measurement. Before X-ray irradiation, only the emission peaks related to Eu^{3+} are visible (see **Figure 3**a-3c). Upon X-ray irradiation, a new emission band related to Eu^{2+} appears and the intensity increases with X-ray irradiation time. To better visualize the photoluminescence change, the integrated emission intensities of Eu^{2+} ($\boldsymbol{I}_{\mathbf{Eu^{2+}}}$) and Eu^{3+} ($\boldsymbol{I}_{\mathbf{Eu^{3+}}}$) as a function of X-ray irradiation time are presented in Figure 3d and Figure S8. $\boldsymbol{I}_{\mathbf{Eu^{2+}}}$ is integrated in the range of 425-575 nm, 450-575 nm and 500-570 nm for Ba_2SiO_4:Eu, $BaSrSiO_4$:Eu and Sr_2SiO_4:Eu, respectively, while the emission intensity of the $^5D_0 \rightarrow {}^7F_2$ transition is integrated for $\boldsymbol{I}_{\mathbf{Eu^{3+}}}$. For all samples, $\boldsymbol{I}_{\mathbf{Eu^{2+}}}$ increases fast at the beginning of the X-ray irradiation, while $\boldsymbol{I}_{\mathbf{Eu^{3+}}}$ decreases quickly (see Figure 3d and Figure S8). With increasing irradiation time, the rate of the intensity change gradually reduces, and both $\boldsymbol{I}_{\mathbf{Eu^{2+}}}$ and $\boldsymbol{I}_{\mathbf{Eu^{3+}}}$ almost stabilize after 100 min irradiation corresponding to an integrated dose of 1500 Gy. Upon longer irradiation time, the variations of both $\boldsymbol{I}_{\mathbf{Eu^{2+}}}$ and $\boldsymbol{I}_{\mathbf{Eu^{3+}}}$ become small, resulting in inaccurate X-ray dosimetry when detecting $\boldsymbol{I}_{\mathbf{Eu^{2+}}}$ or $\boldsymbol{I}_{\mathbf{Eu^{3+}}}$ but the upper limit dose can be extended to a higher value using the $\boldsymbol{I}_{\mathbf{Eu^{2+}}}/\boldsymbol{I}_{\mathbf{Eu^{3+}}}$ (see Figure 3e). In addition, compared with $BaSrSiO_4$:Eu and Sr_2SiO_4:Eu, Ba_2SiO_4:Eu exhibits the largest

$\boldsymbol{I_{Eu^{2+}}/I_{Eu^{3+}}}$ variation with a more sensitive response to X-ray irradiation (see Figure 3e), making it more suitable for X-ray dosimetry.

The non-linear response is an undesired effect for real-time X-ray dose detection.[59] For Ba_2SiO_4:Eu-based detectors, a linear response in a large dose range (0 - 1500 Gy) can be achieved if the parameter of $I_{Eu^{2+}}/(I_{Eu^{3+}}\text{-}0.0095\times I_{Eu^{2+}})$ is defined as the X-ray response (see Figure S9). However, to be consistent with the method of extracting the green to red pixel intensity ratio from the X-ray image to measure the dose (see below), the parameter of $I_{Eu^{2+}}/I_{Eu^{3+}}$ is adopted as the X-ray response. Although the response of $I_{Eu^{2+}}/I_{Eu^{3+}}$ becomes non-linear under large dose ranges, the $(Ba_{1-x}Sr_x)_2SiO_4$:Eu-based detectors proposed here serve as an integrating X-ray detector or dosimeter. Hence non-linearity can easily be corrected for, provided that the X-ray response is only dependent on the integrated dose and not on the dose rate. As can be seen in Figure 3f and Figure S10a-S10d, this is indeed the case; small variations between the results obtained for different dose rates can be explained by considering that the dose rate is varied but the intensity of the 365 nm excitation light used in between exposures to X-rays remains constant and bleaches the sample. This indicates that the Ba_2SiO_4:Eu detector can indeed be used as an integrating detector and hence the detection limit in terms of the dose rate can be very low as long as the exposure time in the envisioned application is sufficiently long. In addition, a linear X-ray response is observed in the low dose range at different dose rates (see Figure 3g). Even if the X-ray response becomes nonlinear at high X-ray doses, a high accuracy can still be guaranteed after calibrating with the established response curve since the X-ray response is only dependent on the integrated dose and not on the dose rate. To further confirm this, the response behavior of Ba_2SiO_4:Eu was measured for several times under both the same and different excitation intensities (see Figure S10d-S10f). Good repeatability is obtained in Ba_2SiO_4:Eu (see Figure 3h), indicating that an accurate and stable measurement can be guaranteed. The dose sensitivity (S_r) is calculated from the following equation:

$$S_r = \frac{1}{\Delta}\left|\frac{\partial \Delta}{\partial D}\right| \quad (1)$$

where Δ is the integrated photoluminescence intensity ratio between Eu^{2+} and Eu^{3+}, D is the irradiation dose. As shown in Figure 3i, the dose sensitivity is, naturally, also dose-dependent and independent of the dose rate, which is more sensitive in the low dose range and decreases gradually with increasing doses. Although the performance at low integrated X-ray doses still needs to be improved for applications related to, e.g. medical imaging,[60-65] the high radiation resistance and large dose range allow to use Ba_2SiO_4:Eu detectors for applications where high

integrated doses and large dose ranges are encountered such as microbeam radiation therapy, food irradiation and detection of highly radioactively-contaminated areas.[45, 53]

Due to the variation of $\boldsymbol{I_{Eu^{2+}}/I_{Eu^{3+}}}$, a photoluminescence color change is observed in Ba_2SiO_4:Eu, as shown in **Figures 4**a and 4b. When the X-ray irradiation time increases from 0 to ~100 min, the CIE coordinates of Ba_2SiO_4:Eu evolve from (0.562, 0.325) to (0.184, 0.526) and the corresponding emission color (λ_{ex} = 365 nm) gradually shifts from red to green with the most distinct change in the initial 10 min. A similar photoluminescence color change is also observed in $BaSrSiO_4$:Eu and Sr_2SiO_4:Eu but due to the overlap between the emission of Eu^{2+} and Eu^{3+} this is less pronounced, as shown in Figure S11. This large radiation-induced photoluminescence color change in Ba_2SiO_4:Eu makes this material perfectly suited for X-ray imaging by using the photoluminescence color contrast after receiving different X-ray doses. While it is in principle possible to determine the X-ray dose by measuring the change in one of the emission bands (corresponding to Eu^{2+} or Eu^{3+}), this requires both a stable excitation intensity over the same sample area and a reproducible detection of the emission intensity, which is in practice not straightforward. Evaluating the ratio between two emission bands resolves those issues, as the ratio is under typical conditions independent of the excitation intensity or the PL collection efficiency. This is a similar situation as for ratiometric luminescence-based thermometry.[66] The additional advantage in the present case is that both emission bands are well separated, which allows easy detection by eye or by commercial photo cameras. As the data in Figure 4b shows, it is indeed possible to calculate the X-ray dose by analyzing the ratio of the green and red pixel intensities of the image captured with a digital camera removing the need for spectroscopically resolved measurements and hence realizing simultaneous X-ray imaging and dosimetry.

To confirm the feasibility of calculating the X-ray dose from the obtained images, the three primary colors, namely, RGB components (red, green and blue) of the image were extracted from the raw camera data using MATLAB. Here, the photographs of Ba_2SiO_4:Eu in Figure 4b after X-ray irradiation for different times were used. The RGB intensity ratio of green to red (I_G/I_R) as a function of $\boldsymbol{I_{Eu^{2+}}/I_{Eu^{3+}}}$ upon the same X-ray irradiation time was plotted (see Figure 4c). A good linear relationship between the I_G/I_R and $\boldsymbol{I_{Eu^{2+}}/I_{Eu^{3+}}}$ is obtained. Using the relationship between $\boldsymbol{I_{Eu^{2+}}/I_{Eu^{3+}}}$ and X-ray dose (see Figure 3e), the X-ray dose-dependent I_G/I_R is established in Figure 4d. Therefore, it is possible to calculate the X-ray dose from the I_G/I_R information of the image. As a result, simultaneous X-ray imaging and dosimetry can be achieved in Ba_2SiO_4:Eu-based detectors. The memory stability and cycling robustness of the detector also need to be considered for practical applications. Figure 4e shows the PL spectra

of irradiated Ba_2SiO_4:Eu after waiting different times in a dark environment. The attenuation of the PL intensity is less than 5 % in 12 hours, confirming good stability. Furthermore, the irradiated sample can be switched to its original state upon 420 nm illumination and then used again (see Figure 4f). The cycling robustness of Ba_2SiO_4:Eu is evaluated by measuring the PL spectra upon alternate 100 min X-ray irradiation and 30 min 420 nm illumination. During five cycles, the PL intensity of Ba_2SiO_4:Eu at 520 nm remains stable for both the irradiated state and the bleached state (see Figure 4g), showing good cycle stability. The reversible valence change between Eu^{3+} and Eu^{2+} is similar to what is observed in certain (persistent) luminescent materials. In these materials the charge transfer usually takes place between Eu^{2+} and a trivalent lanthanide co-dopant (Ln^{3+}). The oxidation of the Eu^{2+} (and simultaneous reduction of the co-dopant) is achieved through excitation of the Eu^{2+} while the reverse charge transfer, i.e. the reduction of Eu^{3+} (and simultaneous oxidation of the co-dopant) can usually be achieved via excitation of the reduced co-dopant (Ln^{2+}). This mechanism has already been verified for CaF_2:Eu,Sm,[47] $SrAl_2O_4$:Eu,Sm[67] and $Sr_4Al_{14}O_{25}$:Eu,Dy[46] where the valence changes of the dopants under illumination with the appropriate wavelength light were confirmed using X-ray absorption spectroscopy. For Ba_2SiO_4:Eu, the reduction to Eu^{2+} is achieved under X-ray exposure. This is most likely because the creation of electron-hole pairs after absorption of an X-ray photon is followed by the electron being trapped at Eu while the hole is presumably trapped at an unknown defect D according to the following redox reaction:

$$Eu^{3+} + D^{Q} \xrightarrow{\text{X-rays}} Eu^{2+} + D^{Q+1} \quad (2)$$

where Q is the original charge state of the hole-trapping defect. In analogy to the process observed in other phosphors, it can be expected that this charge transfer can be reversed through excitation of either of the two newly created defects (i.e. Eu^{2+} or D^{Q+1}). As shown in Figure 2d, the absorption of Eu^{2+} is located between 250 and 450 nm while a comparison of the reflectivity of the material (see Figure S12) before and after X-ray exposure appears to suggest that the absorption of the D^{Q+1} defect is located between 350 and 750 nm. Based on the observation that it is not possible to revert the sample to its original state using cyan (490 nm) or red (620 nm) light while it is possible using violet (420 nm) light, it appears that the reduction of the Eu after X-ray exposure can be reversed through excitation of Eu^{2+}.

Compared with flat-panel X-ray detectors, flexible detectors exhibit obvious advantages in directly imaging irregular objects. Here, a proof-of-concept flexible detector was fabricated by incorporating Ba_2SiO_4:Eu fine powders into a polydimethylsiloxane (PDMS) sheet. As shown in **Figure 5**a, a Ba_2SiO_4:Eu-based sheet was used to image a standard X-ray test pattern plate. The X-ray image of the test pattern plate is presented in Figure 5b. To characterize the

spatial resolution, the I_G/I_R values at different resolution positions were extracted (see Figure 5c), in which the resolution limit can be observed at around 4 lp mm^{-1}. The spatial resolution achieved in Ba_2SiO_4:Eu-based detectors is comparable to that of some commercial X-ray storage phosphor-based detectors (CsBr:Eu^{2+}),[31] organometallic perovskites-based detectors ($CH_3NH_3PbI_3$),[18] and lead-free halide perovskite-based detectors ($(C_8H_{20}N)_2MnBr_4$),[68] but not comparable to that of halide perovskite nanocrystalline or quantum dots-based detectors ($CsPbBr_3$ quantum dots and $CsPbBr_3$ nanocrystals).[10, 17, 69, 70] It should be mentioned that the spatial resolution can be further optimized by decreasing the grain size of Ba_2SiO_4:Eu or tailoring the refractive index matching between the active material and the polymer.[31]

A capsule containing a metal spring and a microchip were used for the imaging demonstration (see Figure 5d and 5e). The object was placed between the X-ray source and the flexible detectors during imaging processes. Before imaging, the flexible plate emits uniform red light upon 365 nm illumination (see Figure 5f), ascribed to the $^5D_0 \rightarrow {}^7F_J$ (J=0, 1, 2, 3, 4) transitions of Eu^{3+}. When exposed to X-rays, the flexible plate under the metal structure receives fewer X-rays because the metal structure exhibits a higher attenuation effect in comparison with the encapsulation case, therefore forming Eu^{2+} spatial concentration contrast in the image plate. Subsequently, the Eu^{2+} spatial concentration contrast was translated into images using the photoluminescence difference of Eu^{2+} and Eu^{3+} under UV illumination. As Figure 5g presents, the inner structure of the microchip is displayed on the plate under 365 nm illumination, which can be directly observed by the naked eye. To evaluate the image retention ability, the X-ray exposed plate was maintained in a dark environment and at room temperature for different times and then read out again. Figure 5h and 5i display the X-ray image of the microchip after waiting 10 days and 28 days, respectively. Although the contrast of the image slightly weakens with increasing waiting time, the imaging information is still well preserved even after waiting 28 days, demonstrating excellent information memory stability. Using a similar process, the capsule was also imaged on the flexible sheet, exhibiting a high contrast and a good spatial resolution (see Figure 5j). Furthermore, the radiation dose generated by the X-ray source relative to air absorption (see Figure 5k) is calculated based on the relationship established in Figure 4d, showing the ability of simultaneous X-ray imaging and dosimetry.

The exposure-time-dependent imaging quality and the accuracy of calculating irradiation dose with our method were evaluated by imaging the same object with different exposure times and a fixed dose rate of ~29 Gy min^{-1} (see Figure S13). Both the contrast between the capsule and spring and the contrast between the capsule and the uncovered area can be influenced by the X-ray exposure time. As the exposure time increases, the contrast between the capsule and

the inner spring gradually increases (see Figure S13a-S13c), but too long exposure time will cause the color of the capsule and the uncovered area to be relatively close (see Figure S13d), which is not conducive to clearly imaging the capsule outline. Therefore, an appropriate exposure time is required to ensure that the obtained images exhibit good resolution and high contrast. The calculated dose generated by the X-ray source relative to air absorption is shown in Figure S13e-S13h. Since the distance between each part of the sheet and the X-ray source is slightly different and some parts of the sheet are covered or blocked by the detected object, the calculated dose value at different parts of the sheet is different. Here the regions with relatively high radiation doses at the edge of the sheet were selected to calculate the generated dose by the X-ray source during imaging processes. The calculated dose ranges from 2 - 3.5 Gy, 4.5 - 6.5 Gy, 8.5 - 12 Gy and 50 - 70 Gy for 5 s, 15 s, 30 s and 120 s irradiation, respectively. The accuracy of the dose value obtained by our method is acceptable if comparing it with the value obtained from the dose rate of the X-ray source. In addition, the flexibility of Ba_2SiO_4:Eu-based detectors was tested according to the procedure shown in Figure S14a. The detector maintains its initial performance without fracture even after bending at 90°, showing the ability to directly image irregular objects. To confirm this, the detector was used to image a wire working in a bending state (see Figure S14b). The obtained X-ray image clearly shows the inside structure of the wire (see Figure S14c). The performance of Ba_2SiO_4:Eu-based detectors after bending for numerous times was also evaluated. Detailed bending processes are provided in Movie-1 (Supporting Information) for 200 times and Movie-2 (Supporting Information) for 400 times. As shown in Figure S14d and S14e, the obtained X-ray images exhibit a good resolution and contrast without any degradation after bending for different times, demonstrating the great potential for flexible imaging. Figure S15 shows the X-ray linear attenuation coefficient of human adipose tissue, muscle-skeletal, Ba_2SiO_4 and C_2H_6OSi.[71, 72] For medical diagnostics and radiation therapy, the X-ray machine usually operates in the range of 50 kV - 150 kV, depending on the type of imaging targets.[14, 31] In this range, the linear absorption coefficient of the image plate can be adjusted to be equivalent to that of muscle-skeletal through tuning the volume ratio between Ba_2SiO_4 and C_2H_6OSi. This behavior makes it possible to evaluate the absorbed radiation dose of human tissue during X-ray radiation therapy processes, which is highly desirable in patient-centered radiography and might promote some new application fields.

3. Conclusion

In this work, we provide a route to design phosphor-based flexible X-ray detectors featuring low cost, simple configuration and convenient readout processes based on radiation-modulated luminescence behavior. The method was validated in the system of $(Ba_{1-x}Sr_x)_2SiO_4$:Eu by using radiation induced valence change of Eu^{3+} towards Eu^{2+}. Upon X-ray irradiation, part of the Eu^{3+} in Ba_2SiO_4:Eu is reduced to Eu^{2+}, forming a new type of luminescent center. The radiation dose-dependent PL intensity of Eu^{2+}/Eu^{3+} and the corresponding strong photoluminescence color change from red to green were employed for simultaneous X-ray dosimetry and imaging. The imaged information using Ba_2SiO_4:Eu detectors can be maintained for more than 28 days and read out easily upon 365 nm illumination without the assistance of other complicated instruments, showing the features of high memory stability and convenient readout processes. The dose can be extracted in a ratiometric way from two well separated spectral regions, avoiding the need for absolute intensity measurements. Spatial variations in the irradiation dose can be assessed *in situ* from the emission color, both visually and from straightforward processing of photo camera images. These excellent performances endow Ba_2SiO_4:Eu with great promise in microbeam radiation therapy and industrial crack detection. More importantly, this work offers a general guideline to design high-performance flexible X-ray detectors with high memory stability and convenient readout processes and promotes the research of phosphor-based X-ray detection technology.

4. Experimental Section

Sample Preparation: $Ba_{1.98}Eu_{0.02}SiO_4$, $Ba_{0.99}Sr_{0.99}Eu_{0.02}SiO_4$ and $Sr_{1.98}Eu_{0.02}SiO_4$ ($(Ba_{1-x}Sr_x)_2SiO_4$:Eu (x=0, 0.5, 1)) were prepared by a conventional solid-state reaction. $BaCO_3$ (Alfa Aesar, 99.8%), $SrCO_3$ (Alfa Aesar, 99.99%), SiO_2 (Alfa Aesar, 99.5%) and Eu_2O_3 (Alfa Aesar, 99.99%) were selected as raw materials without further purification and weighed according to the chemical formula. 10 mol% of H_3BO_3 was added as the sintering aid. After ball milling with ethanol for 8 h at a rotating speed of 300 rpm min^{-1}, the materials were dried in an oven at 60 ℃. Then, the powders were mixed with a polyvinyl alcohol solution (5 wt%) and pressed into pellets with a thickness of ~1 mm and diameter of 13 mm. Finally, the green pellets of Ba_2SiO_4:Eu, $BaSrSiO_4$:Eu and Sr_2SiO_4:Eu were sintered at 1200 °C, 1350 °C and 1450 °C for 5 h, respectively, to obtain dense ceramics. For flexible image sheets, the dense ceramics were first ground into fine powders in a mortar and then incorporated into a silicone elastomer (Sylgard 184) with a weight ratio of 1:5. After mixing uniformly through grinding the mixtures, the solution was cast on a glass plate followed by carefully removing air bubbles at room

temperature. After evaporation of the solvents at 80 ℃ for 2 h, a flexible phosphor-containing polymer layer was obtained.

Characterization: Powder X-ray diffraction patterns were measured using a Siemens D5000 diffractometer (40 kV, 40 mA) with Cu Kα1 radiation (λ = 0.154 nm). The microstructure was measured by using a Hitachi S-3400N microscope, connected to a Thermo Scientific Noran 7 EDX analysis system, under a pressure of 25 Pa and an accelerating voltage of 20 kV. Steady state photoluminescence emission (PL) and excitation (PLE) spectra were performed using an Edinburgh FS920 (Edinburgh Instruments Ltd, Livingston, UK) fluorescence spectrometer. In-situ PL spectra were measured in a home-built setup inside a Siemens D5000 X-ray diffractometer (Cu anode, not filtered) operated at 40 kV, 40 mA; 40 kV, 20 mA; 40 kV, 10 mA and 40 kV, 5 mA, yielding an estimated air kerma rate of 15 Gy min^{-1}, 7.5 Gy min^{-1}, 3.75 Gy min^{-1} and 1.875 Gy min^{-1} at the position of the sample, respectively.[41] The dose rate at the position where studying the exposure-time-dependent imaging quality is ~29 Gy min^{-1}. The emission spectra were measured by a HR2000+ spectrometer (Ocean Optics; Largo, FL, USA). A light emitting diode (centered at 365 nm, full width at half maximum of 16 nm) equipped with a bandpass filter was used as the excitation source for in-situ PL measurement. Two shutters were controlled by a LabVIEW program to alternately open and block the X-ray source and the 365 nm LED. The spectrometer was activated to collect the emission spectrum when the sample was excited by 365 nm LED. The power density of the excitation source for x = 0, 0.5 and 1 is 0.85 mW cm^{-2}, 0.95 mW cm^{-2} and 3.21 mW cm^{-2}, respectively. Optical bleaching experiments were performed using a light emitting diode centered at 420 nm (64 mW cm^{-2}). A S401C thermal power sensor (Thorlabs) was used to measure the intensity of the illumination sources. The reflectivity was measured using a PerkinElmer Lambda1050 UV-vis-NIR spectrophotometer equipped with a Spectralon-coated integrating sphere with PMT (photomultiplier) and InGaAs detectors. Photographs for the X-ray imaging experiment were taken with a Nikon D3200 camera (Nikon Corporation; Tokio, Japan) in raw format. Electron paramagnetic resonance (EPR) measurements were measured on a Bruker ElexSys E500 spectrometer operating at Q-band (34 GHz) and room temperature with 5 mW microwave power. A Pendulum CNT-90XL frequency counter was used to measure microwave frequency and a Bruker NMR ER 035M Gaussmeter for magnetic field. All spectra were normalized to 34 GHz frequency. Field modulation was applied at 100 kHz with an amplitude of 0.3 mT.

Statistical Analysis: The grain size was calculated using the software "Nano Measurer" and all the grains in the image were counted to ensure the reliability of the statistical results. The RGB (red, green and blue) values of the photograph were extracted using the software of MATLAB

and the powder EPR simulation was performed with the EasySpin libraries in MATLAB. The emission spectra measured by the HR2000+ spectrometer were calibrated with an LS-1-CAL Calibrated Light Source (Ocean Optics; Largo, FL, USA) and a background measured with the same integrated time in a dark environment was subtracted. For calculating radiation dose from the photograph, a background image from an unirradiated sheet taken under the same condition was subtracted. For different cycle measurements, the initial state of the sample (before X-ray irradiation) was corrected to the same state.

Supporting Information

Supporting Information is available from the Wiley Online Library or from the author.

Acknowledgements

The authors acknowledge the financial support from the FWO (Fund for Scientific Research – Flanders, projects I002418N and G0F9322N). The authors thank Luc Van Hoorebeke of Centre for X-ray Tomography, Ghent University for providing the standard X-ray test pattern plate.

Conflict of Interest

The authors declare no conflict of interest.

Received: ()

Revised: ()

Published online: ()

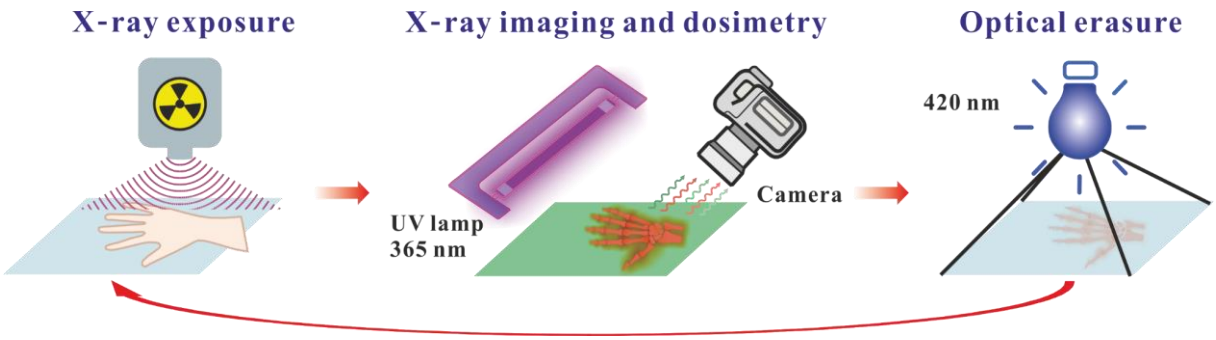

Figure 1. Schematic diagram of the X-ray imaging and dosimetry processes using $(Ba_{1-x}Sr_x)_2SiO_4$:Eu-based detectors. Under 365 nm excitation, the luminescence color changes from red (areas not exposed to X-rays) to green (for the highest X-ray dose). Using 420 nm light, the sample can be bleached and re-used.

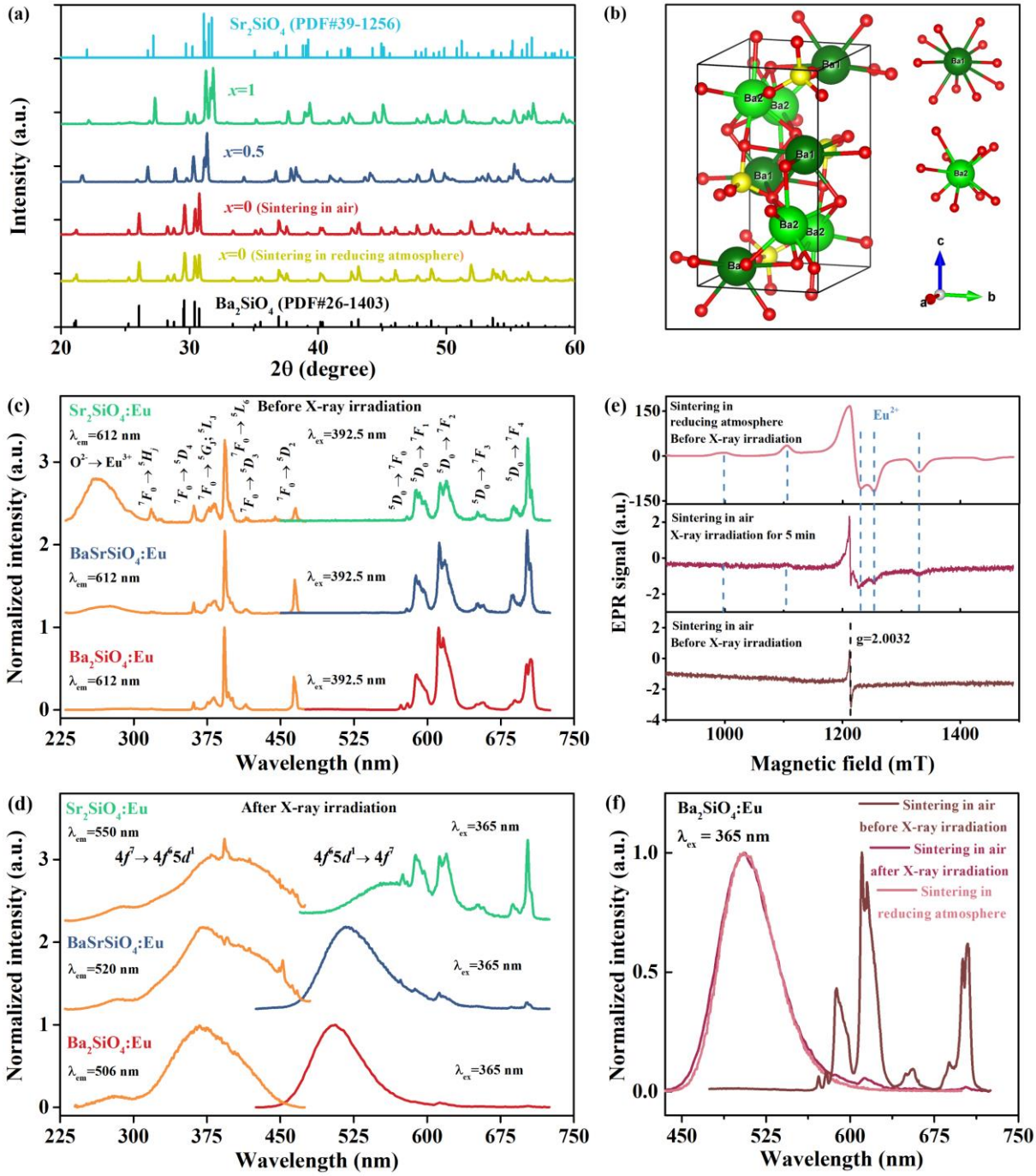

Figure 2. a) XRD patterns of $(Ba_{1-x}Sr_x)_2SiO_4$:Eu phosphors. b) Crystal structure of Ba_2SiO_4. c) Normalized PLE (λ_{em} = 612 nm) and PL (λ_{ex} = 392.5 nm) spectra of $(Ba_{1-x}Sr_x)_2SiO_4$:Eu phosphors before X-ray irradiation. d) Normalized PLE (λ_{em} = 506 nm for Ba_2SiO_4:Eu, λ_{em} = 520 nm for $BaSrSiO_4$:Eu and λ_{em} = 560 nm for Sr_2SiO_4:Eu) and PL (λ_{ex} = 365 nm) spectra of $(Ba_{1-x}Sr_x)_2SiO_4$:Eu phosphors after X-ray irradiation for 100 min. e) EPR spectra of Ba_2SiO_4:Eu samples sintered in air before and after X-ray irradiation for 5 min, and Ba_2SiO_4:Eu samples sintered in reducing atmosphere without X-ray irradiation. f) Normalized PL (λ_{ex} = 365 nm) spectra of Ba_2SiO_4:Eu phosphors sintered in reducing atmosphere, sintered in air before X-ray irradiation and sintered in air after X-ray irradiation for 100 min.

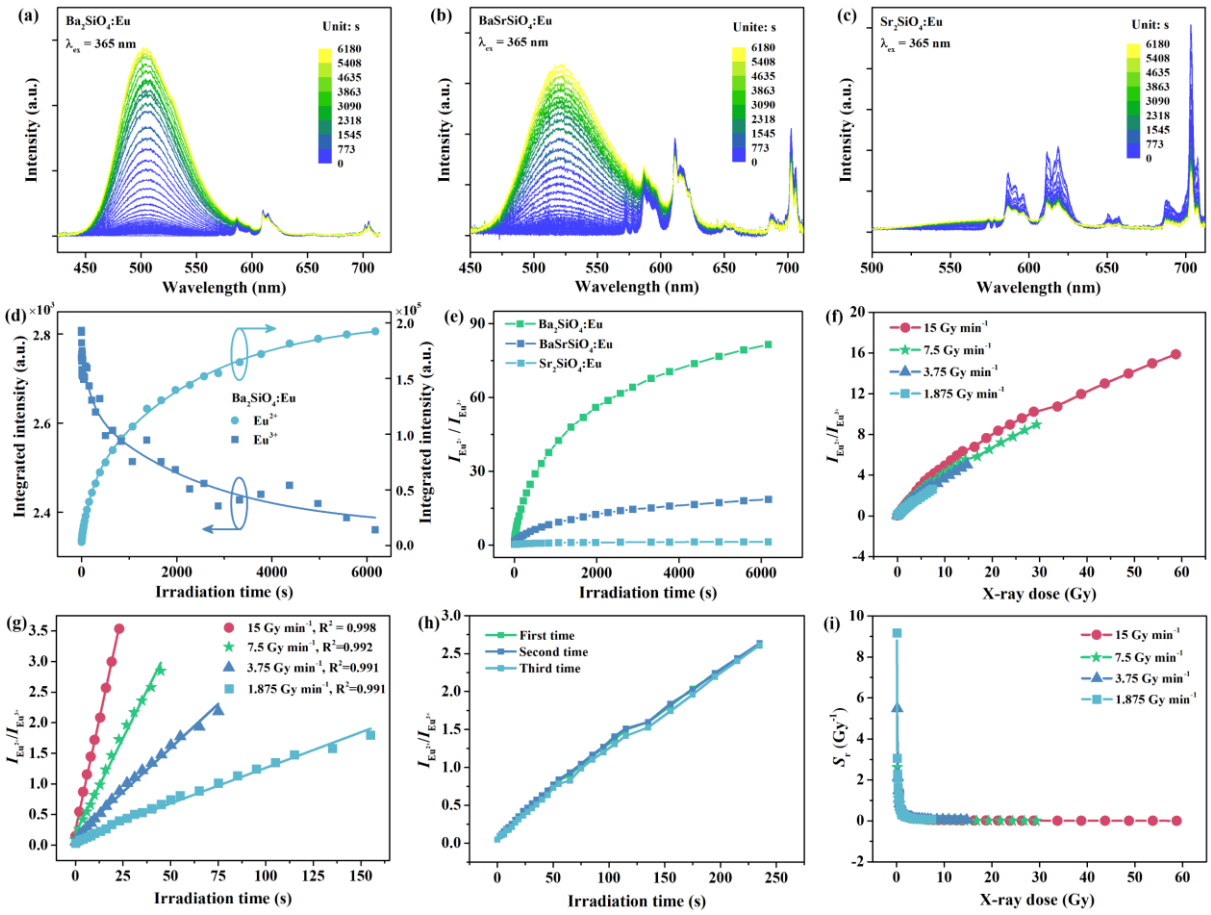

Figure 3. In-situ PL (λ_{ex} = 365 nm) spectra of a) Ba_2SiO_4:Eu, b) $BaSrSiO_4$:Eu and c) Sr_2SiO_4:Eu phosphors after different X-ray irradiation times. d) Dependence of the integrated photoluminescence intensity of Eu^{2+} and Eu^{3+} of Ba_2SiO_4:Eu phosphors as a function of X-ray irradiation time. e) Dependence of the $I_{Eu^{2+}}/I_{Eu^{3+}}$ of $(Ba_{1-x}Sr_x)_2SiO_4$:Eu as a function of X-ray irradiation time. f) Dependence of the $I_{Eu^{2+}}/I_{Eu^{3+}}$ of Ba_2SiO_4:Eu as a function of irradiation dose under different X-ray dose rates. Dependence of the $I_{Eu^{2+}}/I_{Eu^{3+}}$ of Ba_2SiO_4:Eu as a function of X-ray irradiation time g) under different X-ray dose rates and h) for different cycle measurements. i) Dose sensitivity of Ba_2SiO_4:Eu as a function of irradiation dose under different X-ray dose rates.

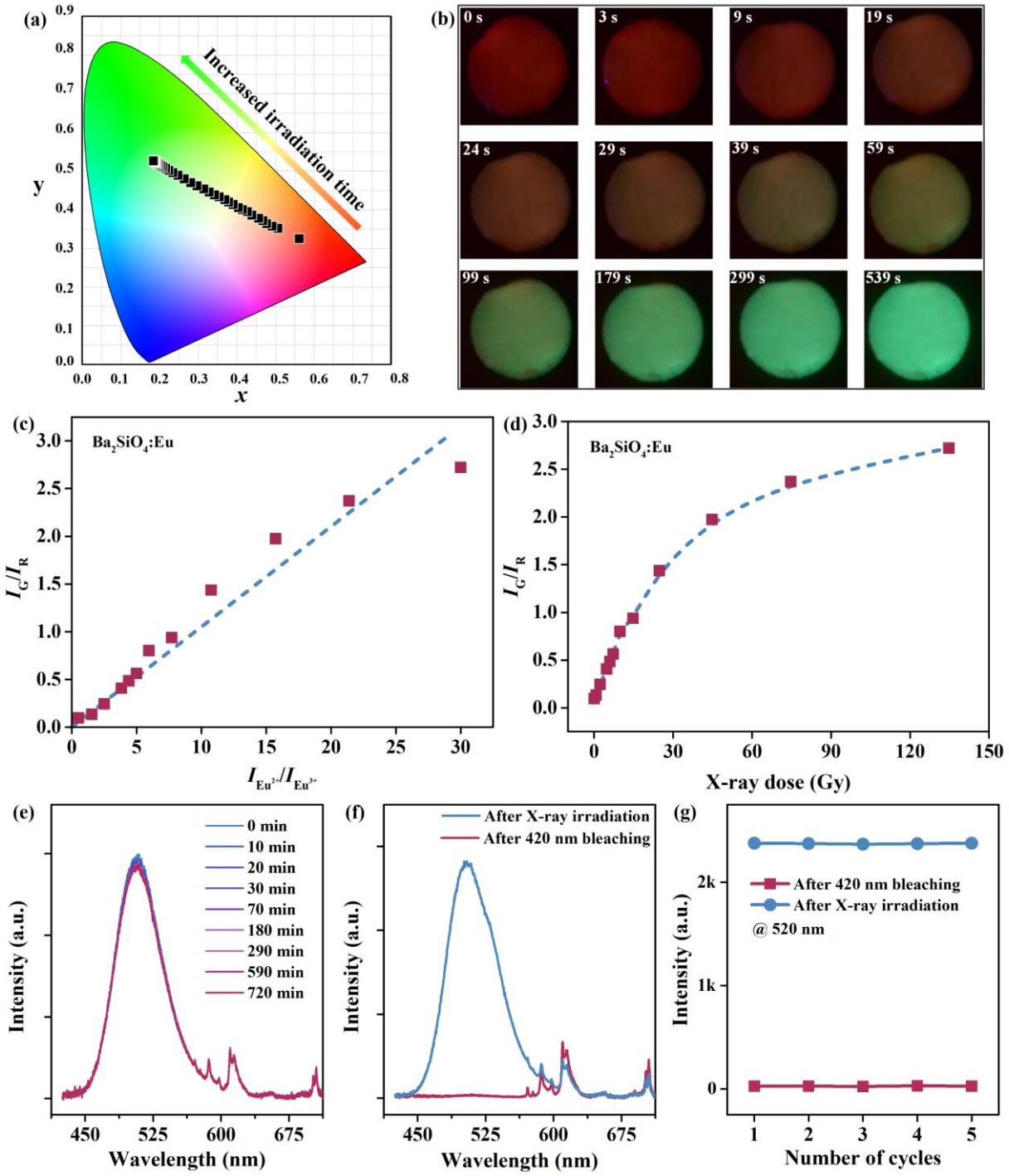

Figure 4. a) The CIE 1931 chromaticity diagram of Ba_2SiO_4:Eu as a function of irradiation time. b) Photographs of Ba_2SiO_4:Eu under 365 nm illumination after different X-ray irradiation times. c) The ratio I_G/I_R for the green over red pixel intensities as derived from the photographs, as a function of $I_{Eu^{2+}}/I_{Eu^{3+}}$ for Ba_2SiO_4:Eu after X-ray irradiation for different times. d) I_G/I_R as a function of X-ray doses for Ba_2SiO_4:Eu after X-ray irradiation for different times. e) PL spectra (λ_{ex} = 365 nm) of irradiated Ba_2SiO_4:Eu at room temperature after waiting different times. f) PL spectra (λ_{ex} = 365 nm) of Ba_2SiO_4:Eu after X-ray irradiation for 100 min and after

420 nm bleaching for 30 min. g) PL intensity (λ_{ex} = 365 nm) of Ba_2SiO_4:Eu at 520 nm upon alternate X-ray irradiation and 420 nm bleaching for 5 cycles.

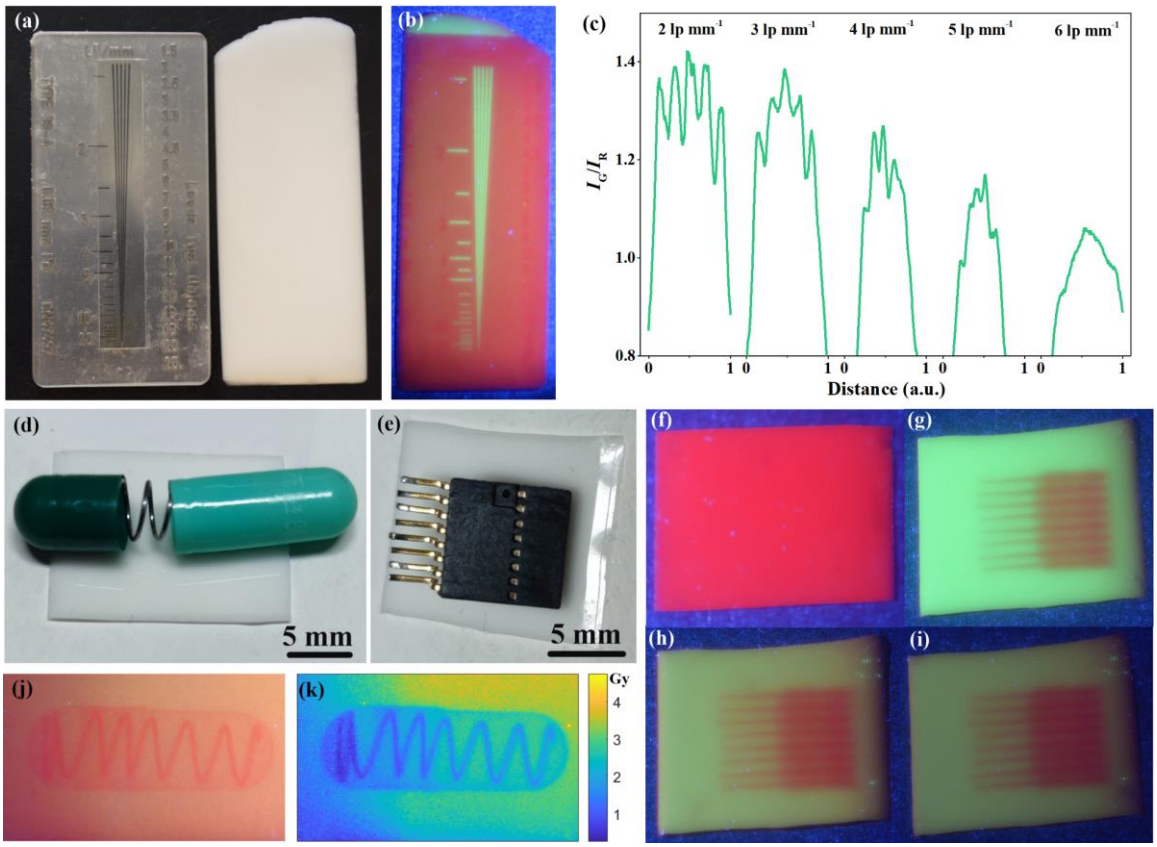

Figure 5. a) Bright field photographs of a standard X-ray test pattern plate and an image sheet. b) The X-ray image of the test pattern plate. c) The extracted I_G/I_R values at different resolution positions. Photographs of d) a capsule containing a spring inside in open state and e) a microchip. f) Photograph of the flexible image plate under 365 nm illumination before X-ray irradiation. g) Obtained X-ray image of the microchip. The X-ray images of the microchip after waiting h) 10 days and i) 28 days at room temperature in the dark. j) Obtained X-ray image of the capsule and k) the calculated irradiation dose at different locations relative to air absorption during the imaging process.

References

[1] M.R. Ay, M. Shahriari, S. Sarkar, M. Adib, H. Zaidi, *Phys. Med. Biol.* **2004**, *49*, 4897.
[2] R. Hanke, T. Fuchs, N. Uhlmann, *Nucl. Instrum. Meth. A* **2008**, *591*, 14.
[3] L. Borgese, F. Bilo, R. Dalipi, E. Bontempi, L.E. Depero, *Spectrochim. Acta B* **2015**, *113*, 1.
[4] M.P. Morigi, F. Casali, M. Bettuzzi, R. Brancaccio, V. D'Errico, *Appl. Phys. A* **2010**, *100*, 653.
[5] J.H. Heo, D.H. Shin, J.K. Park, D.H. Kim, S.J. Lee, S.H. Im, *Adv. Mater.* **2018**, *30*, 1801743.

[6] S. Shrestha, R. Fischer, G.J. Matt, P. Feldner, T. Michel, A. Osvet, I. Levchuk, B. Merle, S. Golkar, H. Chen, S.F. Tedde, O. Schmidt, R. Hock, M. Rührig, M. Göken, W. Heiss, G. Anton, C.J. Brabec, *Nat. Photonics* **2017**, *11*, 436.
[7] W. Yuan, G. Niu, Y. Xian, H. Wu, H. Wang, H. Yin, P. Liu, W. Li, J. Fan, *Adv. Funct. Mater.* **2019**, *29*, 1900234.
[8] H.M. Thirimanne, K. Jayawardena, A.J. Parnell, R.M.I. Bandara, A. Karalasingam, S. Pani, J.E. Huerdler, D.G. Lidzey, S.F. Tedde, A. Nisbet, C.A. Mills, S.R.P. Silva, *Nat. Commun.* **2018**, *9*, 2926.
[9] T. Takahashi, S. Watanabe, *IEEE T. NucL. Sci.* **2001**, *48*, 950.
[10] W. Ma, T. Jiang, Z. Yang, H. Zhang, Y. Su, Z. Chen, X. Chen, Y. Ma, W. Zhu, X. Yu, H. Zhu, J. Qiu, X. Liu, X. Xu, Y.M. Yang, *Adv. Sci.* **2021**, *8*, 2003728.
[11] W. Pan, H. Wu, J. Luo, Z. Deng, C. Ge, C. Chen, X. Jiang, W.-J. Yin, G. Niu, L. Zhu, L. Yin, Y. Zhou, Q. Xie, X. Ke, M. Sui, J. Tang, *Nat. Photonics* **2017**, *11*, 726.
[12] K.S. Shah, R.A. Street, Y. Dmitriyev, P. Bennett, L. Cirignano, M. Klugerman, M.R. Squillante, G. Entine, *Nucl. Instrum. Meth. A* **2001**, *458*, 140.
[13] M.Z. Kabir, S.O. Kasap, *Appl. Phys. Lett.* **2002**, *80*, 1664.
[14] A. Ciavatti, R. Sorrentino, L. Basiricò, B. Passarella, M. Caironi, A. Petrozza, B. Fraboni, *Adv. Funct. Mater.* **2021**, *31*, 2009072.
[15] Y. Zhang, R. Sun, X. Ou, K. Fu, Q. Chen, Y. Ding, L.J. Xu, L. Liu, Y. Han, A.V. Malko, X. Liu, H. Yang, O.M. Bakr, H. Liu, O.F. Mohammed, *ACS Nano* **2019**, *13*, 2520.
[16] F. Cao, D. Yu, W. Ma, X. Xu, B. Cai, Y.M. Yang, S. Liu, L. He, Y. Ke, S. Lan, K.L. Choy, H. Zeng, *ACS Nano* **2020**, *14*, 5183.
[17] H. Zhang, Z. Yang, M. Zhou, L. Zhao, T. Jiang, H. Yang, X. Yu, J. Qiu, Y.M. Yang, X. Xu, *Adv. Mater.* **2021**, *33*, 2102529.
[18] Y.C. Kim, K.H. Kim, D.Y. Son, D.N. Jeong, J.Y. Seo, Y.S. Choi, I.T. Han, S.Y. Lee, N.G. Park, *Nature* **2017**, *550*, 87.
[19] H. Wei, Y. Fang, P. Mulligan, W. Chuirazzi, H.-H. Fang, C. Wang, B.R. Ecker, Y. Gao, M.A. Loi, L. Cao, J. Huang, *Nat. Photonics* **2016**, *10*, 333.
[20] S. Yakunin, M. Sytnyk, D. Kriegner, S. Shrestha, M. Richter, G.J. Matt, H. Azimi, C.J. Brabec, J. Stangl, M.V. Kovalenko, W. Heiss, *Nat. Photonics* **2015**, *9*, 444.
[21] W. Zhu, W. Ma, Y. Su, Z. Chen, X. Chen, Y. Ma, L. Bai, W. Xiao, T. Liu, H. Zhu, X. Liu, H. Liu, X. Liu, Y. Yang, *Light-Sci. Appl.* **2020**, *9*, 1.
[22] W. Li, H. Kou, W. Zhang, L. Ge, H. Pan, Z. Hu, Y. Zhang, *Int. J. Appl. Ceram. Technol.* **2019**, *17*, 1440.
[23] L. Lu, M. Sun, Q. Lu, T. Wu, B. Huang, *Nano Energy* **2021**, *79*, 105437.
[24] X. Wang, H. Shi, H. Ma, W. Ye, L. Song, J. Zan, X. Yao, X. Ou, G. Yang, Z. Zhao, M. Singh, C. Lin, H. Wang, W. Jia, Q. Wang, J. Zhi, C. Dong, X. Jiang, Y. Tang, X. Xie, Y. Yang, J. Wang, Q. Chen, Y. Wang, H. Yang, G. Zhang, Z. An, X. Liu, W. Huang, *Nat. Photonics* **2021**, *15*, 187.
[25] X. Qin, X. Liu, W. Huang, M. Bettinelli, X. Liu, *Chem. Rev.* **2017**, *117*, 4488.
[26] J.-X. Wang, X. Wang, J. Yin, L. Gutiérrez-Arzaluz, T. He, C. Chen, Y. Han, Y. Zhang, O.M. Bakr, M. Eddaoudi, O.F. Mohammed, *ACS Energy Lett.* **2021**, *7*, 10.
[27] Y. Zhou, J. Chen, O.M. Bakr, O.F. Mohammed, *ACS Energy Lett.* **2021**, *6*, 739.
[28] J. Liu, B. Shabbir, C. Wang, T. Wan, Q. Ou, P. Yu, A. Tadich, X. Jiao, D. Chu, D. Qi, D. Li, R. Kan, Y. Huang, Y. Dong, J. Jasieniak, Y. Zhang, Q. Bao, *Adv. Mater.* **2019**, *31*, 1901644.
[29] X. Ou, X. Qin, B. Huang, J. Zan, Q. Wu, Z. Hong, L. Xie, H. Bian, Z. Yi, X. Chen, Y. Wu, X. Song, J. Li, Q. Chen, H. Yang, X. Liu, *Nature* **2021**, *590*, 410.
[30] T. Yanagida, G. Okada, N. Kawaguchi, *J. Lumin.* **2019**, *207*, 14.
[31] P. Leblans, D. Vandenbroucke, P. Willems, *Materials* **2011**, *4*, 1034.
[32] A.J.J. Bos, *Radiat. Meas.* **2006**, *41*, S45.
[33] E.G. Yukihara, S.W. McKeever, *Phys. Med. Biol.* **2008**, *53*, R351.

[34] P.A. Jursinic, *Med. Phys.* **2007**, *34*, 4594.
[35] H.v. Seggern, *Braz. J. Phys.* **1999**, *29*, 254.
[36] H. Nanto, T. Usuda, H. Sokooshi, S. Nakamura, K. Inabe, N. Takeuchi, *Sensor. Actuat. B-Chem.* **1993**, *10*, 197.
[37] Y. Liu, Z. Chen, W. Ba, Y. Fan, Q. Guo, X. Yu, A. Chang, W. Lu, Y. Du, *Nucl. Sci. Tech.* **2008**, *19*, 113.
[38] M.S. Akselrod, A.C. Lucas, J.C. Polf, S.W.S. Mckeever, *Radiat. Meas.* **1998**, *29*, 391.
[39] F. Nakamura, T. Kato, G. Okada, N. Kawaguchi, K. Fukuda, T. Yanagida, *J. Eur. Ceram. Soc.* **2017**, *37*, 4919.
[40] M.K. Crawford, L.H. Brixner, *J. Lumin.* **1991**, *48 & 49*, 37.
[41] D. Van der Heggen, D.R. Cooper, M. Tesson, J.J. Joos, J. Seuntjens, J.A. Capobianco, P.F. Smet, *Nanomaterials* **2019**, *9*, 1127.
[42] A. Wambersie, J. Zoetelief, H.G. Menzel, H. Paretzke, *Radiat. Prot. Dosim.* **2005**, *117*, 7.
[43] R.L. Hachadorian, P. Bruza, M. Jermyn, D.J. Gladstone, B.W. Pogue, L.A. Jarvis, *Nat. Commun.* **2020**, *11*, 2298.
[44] S. Yamaguchi, E. Sato, Y. Ieko, H. Ariga, K. Yoshioka, *Rev. Sci. Instrum.* **2021**, *92*, 053103.
[45] M.A. Grotzer, E. Schultke, E. Brauer-Krisch, J.A. Laissue, *Phys. Med.* **2015**, *31*, 564.
[46] J.J. Joos, K. Korthout, L. Amidani, P. Glatzel, D. Poelman, P.F. Smet, *Phys. Rev. Lett.* **2020**, *125*, 033001.
[47] J.J. Joos, D. Van der Heggen, L. Amidani, L. Seijo, Z. Barandiarán, *Phys. Rev. B* **2021**, *104*, L201108.
[48] G. Okada, Y. Fujimoto, H. Tanaka, S. Kasap, T. Yanagida, *J. Mater. Sci: Mater. Electron.* **2017**, *28*, 15980.
[49] N. Chowdhury, N. Riesen, H. Riesen, *J. Phys. Chem. C* **2019**, *123*, 25477.
[50] L. Ma, K. Jiang, X.-t. Liu, W. Chen, *J. Appl. Phys.* **2014**, *115*, 103104.
[51] M.-F. Volhard, T. Jüstel, *Opt. Commun.* **2018**, *410*, 617.
[52] A. Nag, T.R.N. Kutty, *J. Mater. Chem.* **2004**, *14*, 1598.
[53] C.P. Feliciano, *Radiat. Phys. Chem.* **2018**, *144*, 34.
[54] R.D. Shannon, *Acta Cryst.* **1976**, *32*, 751.
[55] L. Lin, L. Ning, R. Zhou, C. Jiang, M. Peng, Y. Huang, J. Chen, Y. Huang, Y. Tao, H. Liang, *Inorg. Chem.* **2018**, *57*, 7090.
[56] K.A. Denault, J. Brgoch, M.W. Gaultois, A. Mikhailovsky, R. Petry, H. Winkler, S.P. DenBaars, R. Seshadri, *Chem. Mater.* **2014**, *26*, 2275.
[57] J.J. Joos, P.F. Smet, L. Seijo, Z. Barandiarán, *Inorg. Chem. Front.* **2020**, *7*, 871.
[58] J. E. Wertz, and J. R. Bolton. Elementary theory and practical applications. New York: McGraw-Hill Book Co., 1972.
[59] F. Zhou, Z. Li, W. Lan, Q. Wang, L. Ding, Z. Jin, *Small Methods* **2020**, *4*, 2000506.
[60] M. Xia, Z. Song, H. Wu, X. Du, X. He, J. Pang, H. Luo, L. Jin, G. Li, G. Niu, J. Tang, *Adv. Funct. Mater.* **2022**, 2110729.
[61] M. Xia, J.H. Yuan, G. Niu, X. Du, L. Yin, W. Pan, J. Luo, Z. Li, H. Zhao, K.H. Xue, X. Miao, J. Tang, *Adv. Funct. Mater.* **2020**, *30*, 1910648.
[62] Q. Chen, J. Wu, X. Ou, B. Huang, J. Almutlaq, A.A. Zhumekenov, X. Guan, S. Han, L. Liang, Z. Yi, J. Li, X. Xie, Y. Wang, Y. Li, D. Fan, D.B.L. Teh, A.H. All, O.F. Mohammed, O.M. Bakr, T. Wu, M. Bettinelli, H. Yang, W. Huang, X. Liu, *Nature* **2018**, *561*, 88.
[63] X. Ou, X. Chen, X. Xu, L. Xie, X. Chen, Z. Hong, H. Bai, X. Liu, Q. Chen, L. Li, H. Yang, *Research* **2021**, *2021*, 9892152.
[64] Z. Lin, S. Lv, Z. Yang, J. Qiu, S. Zhou, *Adv. Sci.* **2022**, *9*, e2102439.
[65] H. Wu, Y. Ge, G. Niu, J. Tang, *Matter* **2021**, *4*, 144.
[66] M. Suta, A. Meijerink, *Adv. Theory Simul.* **2020**, *3*, 2000176.

[67] D. Van der Heggen, R. Zilenaite, E. Ezerskyte, V. Fritz, K. Korthout, D. Vandenberghe, J. De Grave, J. Garrevoet, L. Vincze, D. Poelman, J.J. Joos, P.F. Smet, *Adv. Funct. Mater.* **2021**, 2109635.
[68] T. Jiang, W. Ma, H. Zhang, Y. Tian, G. Lin, W. Xiao, X. Yu, J. Qiu, X. Xu, Y. Yang, D. Ju, *Adv. Funct. Mater.* **2021**, *31*, 2009973.
[69] W.Q. Chen, M. Zhou, Y. Liu, X. Yu, C.J. Pi, Z. Yang, H. Zhang, Z.C. Liu, T. Wang, J.B. Qiu, S.F. Yu, Y. Yang, X.H. Xu, *Adv. Funct. Mater.* **2022**, *32*, 2107424.
[70] L. Xie, Z. Hong, J. Zan, Q. Wu, Z. Yang, X. Chen, X. Ou, X. Song, Y. He, J. Li, Q. Chen, H. Yang, *Adv. Mater.* **2021**, *33*, 2101852.
[71] https://physics.nist.gov/PhysRefData/XrayMassCoef/tab4.html.
[72] https://physics.nist.gov/PhysRefData/FFast/html/form.html.

Z. Yang, J. Hu, D. Van der Heggen*, A. Feng, H. Hu, H. Vrielinck, P. F. Smet, D. Poelman*

Realizing simultaneous X-ray Imaging and Dosimetry using Phosphor-based Detectors with High Memory Stability and Convenient Readout Process

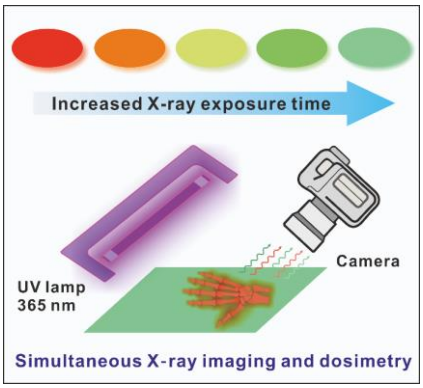

This study presents an approach to develop phosphor-based X-ray detectors with high memory stability and convenient readout processes using radiation-induced photoluminescence tuning in $(Ba_{1-x}Sr_x)_2SiO_4$:Eu phosphors. The associated photoluminescence change and the accompanying color contrast in response to the radiation dose are exploited for simultaneous X-ray imaging and dosimetry, showing great potential for large dose range or high dose rate radiography.